Signatures of Helium Continuum in Cool Flare Loops Observed by SDO/AIA

Petr Heinzel[1] , Pavol Schwartz[2] , Juraj Lörinčík[1,3] , Július Koza[2] , Sonja Jejčič[1,4,5] , and David Kuridze[6]
[1] Astronomical Institute, The Czech Academy of Sciences, 25165 Ondřejov, Czech Republic; pheinzel@asu.cas.cz
[2] Astronomical Institute, Slovak Academy of Sciences, 05960 Tatranská Lomnica, Slovakia
[3] Astronomical Institute, Faculty of Mathematics and Physics, Ke Karlovu 2027/3, 12116 Praha, Czech Republic
[4] Faculty of Education, University of Ljubljana, Kardeljeva ploščad 16, 1000 Ljubljana, Slovenia
[5] Faculty of Mathematics and Physics, University of Ljubljana, Jadranska 19, 1000 Ljubljana, Slovenia
[6] Department of Physics, Aberystwyth University, Ceredigion SY23 3BZ, UK
Received 2020 January 18; revised 2020 May 26; accepted 2020 May 30; published 2020 June 17

Abstract

We present an analysis of off-limb cool flare loops observed by the Solar Dynamics Observatory (SDO)/ Atmospheric Imaging Assembly (AIA) during the gradual phase of SOL2017-09-10T16:06 X8.2-class flare. In the extreme-ultraviolet (EUV) channels starting from the 335 Å one, cool loops appear as dark structures against the bright loop arcade. These dark structures were precisely coaligned (spatially and temporally) with loops observed by Swedish Solar Telescope (SST) in emission lines of hydrogen and ionized calcium. A recently published semi-empirical model of cool loops based on SST observations serves to predict the level of hydrogen and helium recombination continua. The continua were synthesized using an approximate non-LTE (i.e., departures from local thermodynamic equilibrium) approach and theoretical spectra were then transformed to AIA signals. Comparison with signals detected inside the dark loops shows that only in AIA 211 Å channel the computed level of recombination continua is consistent with observations for some models, while in all other channels that are more distant from the continua edges the synthetic continuum is far too low. In analogy with on-disk observations of flares we interpret the surplus emission as due to numerous EUV lines emitted from hot but faint loops in front of the cool ones. Finally we briefly comment on failure of the standard absorption model when used for analysis of the dark-loop brightness.

Unified Astronomy Thesaurus concepts: Solar flares (1496); Solar coronal loops (1485); Solar extreme ultraviolet emission (1493); Solar flare spectra (1982); Radiative transfer (1335)

1. Introduction

Visibility of dark prominence-like structures above the limb or against the disk in otherwise "hot" extreme-ultraviolet (EUV) channels like those of the Solar and Heliospheric Observatory/EIT, the Transition Region and Coronal Explorer, or now the Solar Dynamics Observatory (SDO)/Atmospheric Imaging Assembly (AIA) was interpreted as the absorption of the background EUV line radiation from hot plasmas by cool prominences. This absorption is due to the photoionization of hydrogen and helium by EUV line photons. Within the above channels, there is a contribution of the hydrogen (Lyman continuum); below 504 Å the neutral helium is added and below 228 Å also ionized helium contributes, but the helium continua dominate in the AIA channels (see Anzer & Heinzel 2005). Many papers analyzed such dark prominences in order to derive their densities proportional to the amount of absorbing material; for a review, see Kucera (2015). Typical prominence densities derived from such diagnostics are in good agreement with those obtained from other analyses. On the other hand, one could also consider the hydrogen and helium continuum *emission* as a result of the photorecombinations, which is the natural process at work. However, as shown by Labrosse et al. (2011), Hinode/EIS prominence spectra do not show any detectable emission in the helium continua below 228 Å. In typical prominence plasmas the electron densities are around 10^{10} cm^{-3}, and this is probably too low for the recombinations to produce the observable continuum emission. Although various studies dealt with hydrogen and helium non-LTE (i.e., departures from local thermodynamic equilibrium)

modeling in prominences (Labrosse 2015), only the line intensities have been presented, no results for helium continua.

Concerning cool flare loops, an appearance of dark loop structures against the bright EUV background was evidenced both from off-limb (Jejčič et al. 2018) as well as on-disk (Song et al. 2016) observations. As noticed in Jejčič et al. (2018), dark loops are clearly visible in SDO/AIA images of 2017 September 10 off-limb flare loop system and we therefore focus in this Letter on their detailed analysis. Our aim is to understand the nature of the dark-loop radiation, which could be at least partially due to helium recombination continua. A similar analysis was carried out in Milligan et al. (2012) and in Milligan & McElroy (2013) for the case of flare ribbons.

Off-limb flare loops are routinely detected in emission in various spectral lines. Recently, Koza et al. (2019) used unique Swedish Solar Telescope (SST) observations of 2017 September 10 flare loops in the hydrogen Hβ and Ca II 8542 Å lines and performed the non-LTE inversions in order to derive the physical parameters of the cool-loop plasma. They arrived at temperatures below 10^4 K, but of great interest are high electron densities around 10^{12} cm^{-3}; these are consistent with those obtained by Jejčič et al. (2018), who analyzed the white-light continuum emission from these loops as detected by SDO/HMI at 6173 Å. We therefore use the model based on SST observations to predict the level of recombination continua below 504 Å (ionization edge of He I) and compare it with AIA observations in five channels, starting with 335 Å. We also briefly comment on the applicability of the absorption model for analysis of the dark-loop brightness.
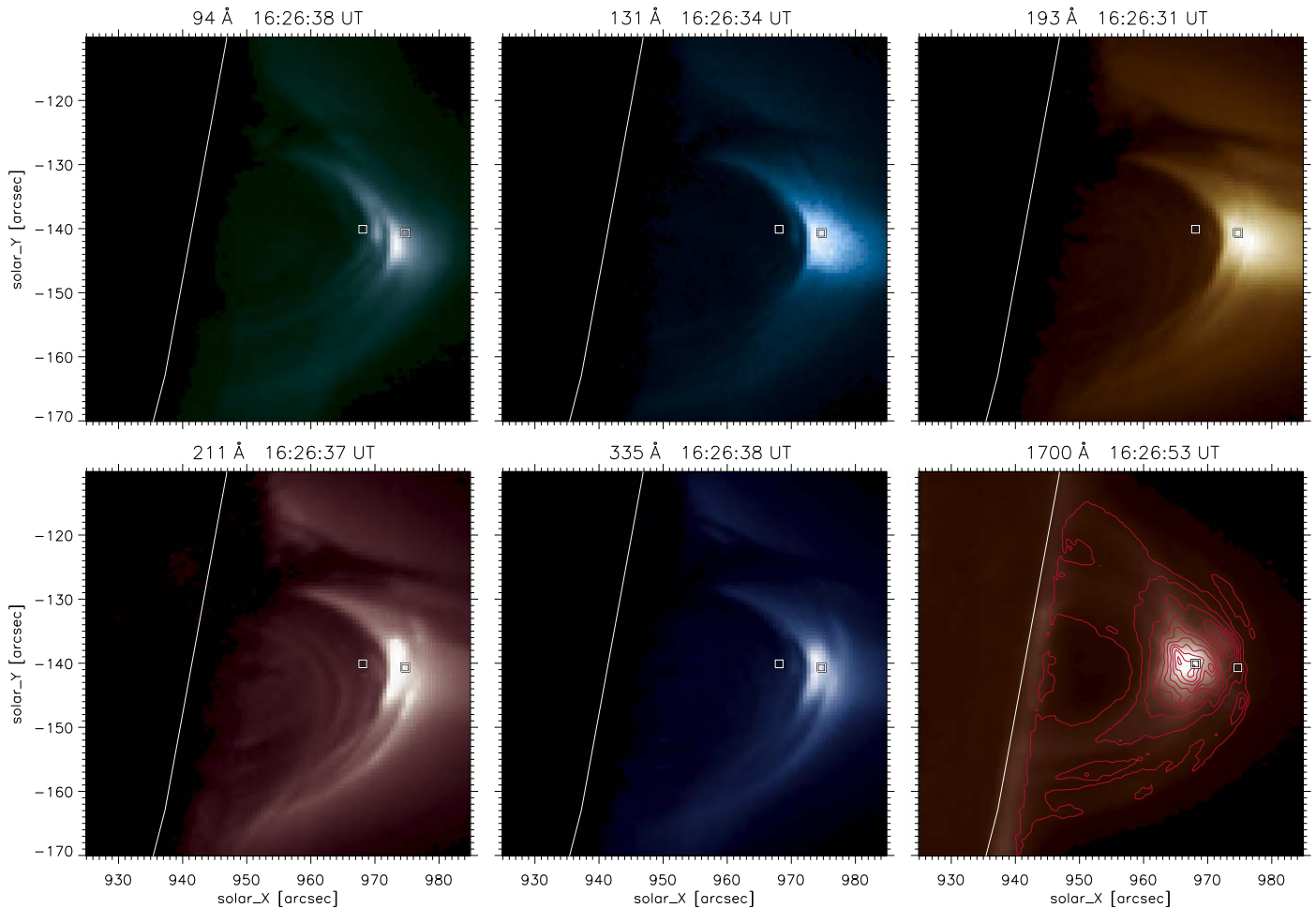
Figure 1. Loop images in six AIA channels. Two areas (boxes) are marked in all images—within dark loops, and within bright loops just above them. The quiet corona was measured at the same height above the limb as the dark-loop box, but far away from the active region. We show here also the image in 1700 Å coaligned with SST observations of cool loops (red contours).

2. Extended Flare Loop System Observed on 2017 September 10

Right after the maximum of the SOL2017-09-10T16:06 X8.2-class flare, various dark loops could be well identified on SDO/AIA images. Here we focus on five AIA channels below the He I continuum edge at 504 Å, where such dark absorbing loops were best visible (Figure 1), and perform their photometric analysis. Observations made by the AIA (Lemen et al. 2012) instrument on board SDO (Pesnell et al. 2012) on 2017 September 10 at 16:26 UT were selected because they are co-temporal with SST imaging spectroscopy used for the non-LTE diagnostics by Koza et al. (2019). In order to avoid saturation, the observations in 94, 131, 193, and 211 Å channels were made in a flare mode with shorter exposures 0.23, 0.015, 0.029, and 0.397 s, respectively, compared to standard ones. However, flare-mode exposures as stored in the headers of the data fits files are sometimes unreliable, and therefore we have calibrated them comparing normal and flare-mode exposures of the off-limb quiet corona. The resulting correction factors to flare-mode exposures are 1.47, 2.28, 2.27, and 1.49 for these four AIA channels, respectively. In the 335 Å channel the standard exposure of 2.9 s was used. Observations in the 171 Å channel are not used because of overexposed pixels. The AIA data were reduced using the standard SolarSoft procedure `aia_prep.pro`. After this basic reduction the data were corrected for internal instrumental scattering with the procedure `aia_deconvolve_richardsonlucy.pro`, which deconvolves the point-spread functions determined for all EUV channels by Poduval et al. (2013) from the observed data. For the deconvolution itself the Richardson–Lucy method was used (Richardson 1972; Lucy 1974). Uncertainties of the observed intensities were calculated using the `aia_bp_estimate_error.pro` routine. In addition, we added to them 28% calibration uncertainty of the instrument (Boerner et al. 2012).

In the AIA images shown in Figure 1 two box-like areas were chosen: one at the top of the system of dark loops, and the second one inside a bright loop just above the apex of the dark-loop system. The dark-loop box was coaligned with SST observations at about the same time (see Section 2.1 below). Average intensities in instrumental units $DN\,s^{-1}\,pix^{-1}$ were obtained from the two areas. The so-called foreground coronal intensity I_f is a contribution to the measured intensity from the corona in front of the loop arcade. Taking into account the fact that geometrical thickness of the loops is negligible as compared to the very extended solar corona, the foreground intensity can be expressed as one half of the intensity of the quiescent corona I_{QS} measured at the same height above the limb as the dark-loop intensity but far enough from the active region. Intensities I_{DL} (dark loop), I_{BL} (bright loop above), and

Table 1
Measured Intensities I_{DL}, I_{BL} and I_{QS} in the Five AIA Channels, with Uncertainties Less than 30%

AIA Channel (Å)	I_{DL} (DN s^{-1} pix^{-1})	I_{BL} (DN s^{-1} pix^{-1})	I_{BL1} (DN s^{-1} pix^{-1})	I_{QS} (DN s^{-1} pix^{-1})
94	10000	67000	20000	250
131	13000	639000	150000	1100
193	39000	1116000	180000	1600
211	5800	70000	20000	300
335	100	1500	1100	5

Note. Positions of the two areas are as follows: the dark-loop area (DL) is located at the position solar_X = +968″ solar_Y = −140″; the bright-loop area (BL) is located just above the dark loops at the position solar_X = +975″ solar_Y = −141″; and the bright-loop areas (BL1) were taken at the same height as the DL box (we use the interpolated value from both sides around the dark loops). The quiet-corona areas (QS) were taken sufficiently far from the active region (out of the frame of our AIA images).

Table 2
Grid of Six Cool-loop SST Models Used to Simulate the AIA Signals

Model	T (kK)	n_H (cm^{-3})	n_e (cm^{-3})	a	b	I_{228} (cgs)	I_{211} (cgs)	I_{335} (AIA)	I_{211} (AIA)	I_{193} (AIA)	τ_{335}	τ_{228}	τ_{211}	τ_{193}
SST-DL	8.7	6.23+12	7.22+11	3.4–1	3.2–3	6.1–12	2.2–14	4.0–5	19.3	3.5–2	1208	641	536	436
SST-BL	8.7	6.23+12	7.22+11	6.6	6.0–2	4.0–10	1.5–12	2.0–4	1264.7	2.3	513	596	486	383
SST-DL-15	15	2.10+12	2.08+12	1.8–1	1.6–3	3.7–12	1.5–13	5.4–2	66.7	2.3	323	178	151	125
SST-BL-15	15	2.10+12	2.08+12	3.4	3.0–2	3.7–10	1.6–11	9.9–1	6926.7	250.1	85	167	138	109
SST-DL-20	20	1.57+12	1.56+12	3.1–1	2.6–3	4.5–12	4.3–13	5.1–1	177.3	17.4	133	132	112	92
SST-BL-20	20	1.57+12	1.56+12	5.6	4.9–2	3.2–10	3.2–11	8.9	13017.0	1325.9	41	122	100	80
HMP7	8	1.00+10	7.10+9	7.7–1	7.1–3	3.6–13	7.7–16	3.6–7	8.6–1	8.3–4	1.8	1.2	1.0	0.8

Note. The models are isothermal-isobaric with a uniform gas pressure p = 9.1 dyn cm^{-2} and microturbulent velocity v_t = 24 km s^{-1}. The thickness of SST models is D = 5100 km. HMP7 is the prominence model of Heasley et al. (1974) shown here for reference, with p = 0.02 dyn cm^{-2}, v_t = 5 km s^{-1} and D = 6000 km. For other quantities see the text. cgs = [erg s^{-1} cm^{-2} sr^{-1} Hz^{-1}], AIA = [DN s^{-1} pix^{-1}].

I_{QS} measured in corresponding boxes in the five AIA channels are shown in Table 1.

As a next step we use the model obtained by Koza et al. (2019) from the non-LTE inversions of lines observed by SST to derive the radiation properties of the cool loops in AIA bands. The densities from the best-fit SST model lead to total optical thicknesses shown in Table 2 (for their evaluation, see the next section). Such very large optical thicknesses clearly indicate that all background EUV radiation, i.e., along the line of sight behind the cool loops, must be totally absorbed. The question then arises: what is the nature of the AIA signal within the cool-loop box? A natural possibility is that the detected emission in dark loops is the radiation of cool loops themselves in the helium recombination continua. This would not be very surprising because of high densities found independently in these loops. For example, in solar prominences having almost two orders of magnitude lower densities than those found in the 2017 September 10 cool loops, the resonance continuum below 228 Å was not detected by Labrosse et al. (2011), who analyzed the Hinode/EIS spectra, although these authors mention some other space observations where such a continuum was present. We therefore perform the theoretical non-LTE synthesis of such continua below 504 Å and compare their intensities with detected AIA signals in all considered channels.

2.1. Spatial Alignment of SDO/AIA and SST Observations

In order to be able to analyze our AIA observations in terms of SST models, we need a careful spatial alignment of AIA and SST images. To co-align the space- and ground-based imagery of the flare loops, the SST/CHROMIS Hβ image in wavelength-integrated intensities is created (see the left panel of Figure 2 in Koza et al. 2019), allowing clearly recognizable common features to be identified in the AIA 1700 Å passband where the cool lines dominate (Jejčič et al. 2018). For the co-alignment the function `auto_align_images.pro` is used, which is implemented within the IDL SolarSoft System (Freeland & Handy 1998). Through the cross-correlation, a satisfactory spatial alignment of co-temporal AIA and SST images is achieved as shown in Figure 1.

3. Synthetic Continuum Intensity

So far no helium continuum intensities have been computed for prominence-like structures including cool flare loops. Heasley et al. (1974, hereafter HMP) and Labrosse & Gouttebroze (2001) presented the results of non-LTE helium line formation under prominence conditions, but they did not synthesize the helium resonance continua. At the wavelengths of interest below 504 Å, three resonance continua are considered: the hydrogen Lyman continuum (head at 912 Å), the He I continuum (head at 504 Å), and the He II continuum (head at 228 Å). The continuum absorption coefficient takes the form (Anzer & Heinzel 2005; Hubeny & Mihalas 2015)

$$\kappa_\nu = \sigma_{H\,I}(\nu)n_{H\,I} + \sigma_{He\,I}(\nu)n_{He\,I} + \sigma_{He\,II}(\nu)n_{He\,II}, \qquad (1)$$

where n is the ground-state population of the respective ion and $\sigma(\nu)$ is the frequency-dependent absorption cross-section for photoionization ($\sigma_{He\,II}(\nu)$ is effective below 228 Å). To compute σ we use standard formulas for hydrogen and He II (Anzer & Heinzel 2005) and the polynomial expansion of

Rumph et al. (1994) for He I. The correction for induced emission is negligible in EUV. The ground states of the respective ions, from which the photoionizations take place, have dominant populations and thus we can replace them with total populations of the ions. Adding the hydrogen continuum opacity computed consistently with the MALI hydrogen non-LTE code (Heinzel 1995; Koza et al. 2019), we get the continuum optical thicknesses presented in Table 2, where τ_{228} is in good agreement with HMP for their model HMP7. An interesting feature here is that the total opacity of helium continua below 228 Å practically does not depend on the ionization structure of helium—this is because both helium cross sections are almost equal close to the continuum head. Then the helium contribution to total τ is proportional only to hydrogen column density (see also Section 5).

The emission coefficient can be expressed according to Hubeny & Mihalas (2015) as

$$\eta_\nu = [\sigma_{\text{H I}}(\nu) n_{\text{H I}}^* + \sigma_{\text{He I}}(\nu) n_{\text{He I}}^* + \sigma_{\text{He II}}(\nu) n_{\text{He II}}^*] B_\nu(T), \quad (2)$$

where we also can neglect the term $(1 - e^{-h\nu/kT})$. Here $n_i^* = n_{i+1} n_e \Phi_i(T)$ are the LTE populations of the ground states of respective ions computed for *actual* electron densities n_e and non-LTE populations n_{i+1} of higher ions, $\Phi_i(T)$ is the Saha–Boltzmann factor and $B_\nu(T)$ the Planck function. Again the last term is effective only below 228 Å. The continuum source function is then $S_\nu = \eta_\nu / \kappa_\nu$, proportional to $B_\nu(T)$ and to n_e. For a given model we compute the electron density (here equal to proton density) and the non-LTE hydrogen ground-state population using the hydrogen code MALI (Heinzel 1995), with partial frequency redistribution in the Lyman lines. The non-LTE populations of He I, He II, and He III ground states (here n_1, n_2, and n_3, respectively) are computed following the approach of Avrett et al. (1976). We write the ionization equilibrium equations for these three helium ions and get the population ratios

$$a = \frac{n_2}{n_1} = \frac{R_{12} + C_{12}}{R_{21}}$$
$$b = \frac{n_3}{n_2} = \frac{R_{23} + C_{23}}{R_{32}}, \quad (3)$$

where R_{12} and R_{23} are the photoionization rates, C_{12} and C_{23} are the collisional ionization rates according to Mihalas & Stone (1968) and Avrett et al. (1976), respectively, and R_{21} together with R_{32} are the radiative recombination rates to all levels of the respective ion (we neglect dielectronic and collisional three-body recombinations). To evaluate the photo-ionization rates we use the above-mentioned cross sections and the external radiation field illuminating the cool loop. The latter is taken from HMP, but was modified below 228 Å where we use the EUV spectral measurements of the quiet Sun from OSO-7 satellite reported by Linsky et al. (1976). All these incident intensities are for quiet-Sun chromospheric and coronal illumination. In order to account for enhanced illumination of the cool loops by surrounding hot EUV loops, we enhance the whole considered spectrum below 504 Å by a certain factor obtained from our AIA measurements (Table 1).

A lower limit is the radiation detected within the dark-loop box, i.e., we assume that the cool SST loop structures can be illuminated by hot loops emitting in front of them (see also the discussion in the next sections). An upper limit is the radiation from hot loops located around the cool ones. We compute the enhancement factors as the ratios $I_{\text{DL}}/(I_{\text{QS}}/2)$ and $I_{\text{BL}}/(I_{\text{QS}}/2)$ which, using data from Table 1, gives averaged values 43 (DL models) and 820 (BL models), respectively. Contrary to Avrett et al. (1976), we ignore here the fact that the incident radiation is partially absorbed at a given atmospheric depth from the surface—our simulations have shown that this effect is of secondary importance in our approximate modeling. As a test case we considered the prominence model HMP7, illuminated by the quiet-Sun radiation. The resulting continuum intensity at 228 Å is 3.6×10^{-13} which fits quite well in the range of OSO-7 prominence observations reported by Linsky et al. (1976). In the present analysis we do not solve the full transfer problem for helium continuum but, observing that τ in Table 2 is very large for all considered models, we use the Eddington–Barbier relation (Hubeny & Mihalas 2015) to estimate the emergent continuum intensity, i.e., $I_\nu \simeq S_\nu$, where the source function is determined at *surface layers* where $\tau_\nu \simeq 1$. This approximation thus works best close to the continuum limit (head); at deeper layers the source function may differ.

In our simulations we consider six loop models (Table 2), based on the best-fit inversion model obtained from the SST spectra (Table 3 in Koza et al. 2019). They are isothermal and isobaric having quasi-constant hydrogen density through the loop thickness D. Surface electron densities n_e are used to compute the synthetic continuum. In our hydrogen code the electron density is equal to proton density and thus the ratio n_e/n_H is the hydrogen ionization degree. We use the original SST cool-loop model and two of its variants with higher temperatures of 15,000 and 20,000 K, simulating cool loops having a transition region to the corona (like prominence-corona transition region, PCTR, in prominences). Each such model has been computed using two limiting enhanced illumination factors. In Table 2 we show the helium ionization ratios a and b and present the synthetic cgs intensities at the head of He II continuum at 228 Å and at 211 Å, two wavelengths representative of the OSO-7 spectra and AIA channel together with Hinode/EIS, respectively. Note a decrease of intensities with increasing temperature at 228 Å, but an increase at 211—this is due to behavior of the helium continuum source function as shown in Avrett et al. (1976). Optical thickness is very large at all considered wavelengths, as shown in Table 2. At 335 Å it represents a lower limit because we do not consider a restricted penetration of the incident EUV radiation into the loop (this is not a problem for wavelengths below 228 Å, where τ is practically insensitive to helium ionization). Note also that the hydrogen Lyman-continuum opacity contributes significantly at low temperatures below 10,000 K. The whole synthetic spectrum is then used to obtain AIA signals in all bands as described in the next section.

4. Comparison with AIA Observations

AIA intensities are in units of DN s^{-1} pix^{-1}, which cannot be directly compared with synthetic intensities expressed in erg s^{-1} cm^{-2} sr^{-1} Hz^{-1} (called cgs units for brevity). This is because the AIA data can hardly be calibrated to these absolute
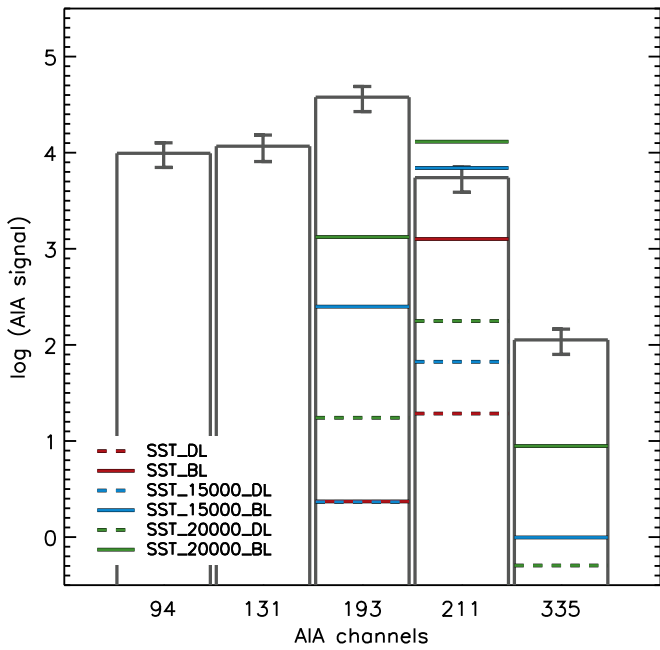
Figure 2. Comparison of the observed and synthetic signals in AIA channels (in $DN\,s^{-1}\,pix^{-1}$ units). Black columns represent the observed signal with corresponding error bars, the synthetic signals from different models are shown as color lines. In two leftmost channels the synthetic signal is too low to be displayed.

energy units. We therefore proceeded in an opposite way and converted the synthetic intensities in cgs units to synthetic $DN\,s^{-1}\,pix^{-1}$ signals, which are readily comparable with observations. To do so, we multiplied the modeled spectra with the response functions of selected filter channels, which we corrected for the sensitivity decay, and with a constant standing for the conversion between the solid angle and AIA pixel. The resulting products were then integrated over the bandpasses of the individual filter channels. Note that the response functions of EUV filter channels are typically broad and those of the 193 and 211 channels cover wavelengths longer than the He II continuum head at 228 Å. Therefore, the spectra were only integrated in wavelength ranges corresponding to 99% of the total observed signal.

Results of the conversion of synthetic spectra into AIA signals are shown in Table 2 and in Figure 2, where the synthetic observables are indicated by color lines. Dashed lines show the lower limit of the AIA signal for the case of DL illumination, while the full color lines represent the upper limit for BL illumination. Note that these signals are dominated by respective helium recombination continua, while the hydrogen Lyman continuum is negligible. Black columns show levels of the observed intensities from Table 1, together with their error bars (after the foreground subtraction). Fast decrease of synthetic continuum intensity with decreasing wavelength (compare channels 211 and 193) is related to behavior of the Planck function in far EUV.

We see that the SST model with BL illumination gives an intensity that is about 20% of the observed one in AIA 211 Å channel, while the same model with DL illumination has a much lower intensity. Comparison in this channel is largely improved if we increase the loop temperature to 15,000 or even 20,000 K, but other channels below 211 Å have intensities still far below the observed ones. We discuss this behavior in the

AIA Channel (Å)	τ	$\sigma_{He\,I}$ (cm²)	N_H (cm⁻²)
94	1.9	⋯	⋯
131	4.0	⋯	⋯
193	3.4	1.19–18	3.0+19
211	2.5	1.44–18	1.9+19
335	2.6	⋯	⋯

Note. N_H is the column density derived from channels 193 and 211 (see the text).

last section. Since we deal here with the surface layers where the 211 Å continuum is formed (due to its large opacity), the enhanced temperature can be representative of a PCTR while the central parts of the loop, if cooler, can still be consistent with the SST model. Note that the SST model is based on lines having a moderate optical thickness and thus being formed deeper, out of PCTR. In Table 2 and Figure 2 we also show the situation in the 335 Å channel, again for the best-fit SST model. The synthetic intensity is much lower in comparison with the AIA signal, similarly as in other AIA channels below 200 Å. The 335 Å channel is already far from the 504 Å continuum head of neutral helium, and thus it is not surprising that the intensity substantially drops. But we see an indication of the 228 Å jump between channels 211 and 335. The reason why the synthetic signals are much lower compared to the observed ones, except for 211 Å channel, is discussed in the last section.

5. Comments on the Standard Absorption Model

In a direct analogy with off-limb prominences one is tempted to apply a standard absorption model to derive the optical thickness of the recombination continua and from that to estimate the density. Assuming that a system of bright loops is located behind the dark ones, and therefore that their intensity measured just above the dark loops is representative of the background EUV radiation (Figure 1 and Table 1), the optical thickness can be calculated as

$$\tau = -\ln\left(\frac{I_{DL} - I_f}{I_{BL}}\right), \quad (4)$$

where $I_f = I_{QS}/2$. Resulting values of τ are shown in Table 3. These values indicate a partial absorption of the background EUV radiation, a standard scenario considered for interpreting dark prominences. Using channels 211 and 193, one can estimate the hydrogen column density N_H in cool loops using the relation (Anzer & Heinzel 2005)

$$N_H = \tau/0.1\sigma_{He\,I}, \quad (5)$$

where $\sigma_{He\,I}$ is the photoionization cross-section of He I (Rumph et al. 1994) and 0.1 is the helium abundance relative to hydrogen. At low temperatures we can neglect the He III ion in estimating total helium density. In this relation we also neglected the hydrogen Lyman-continuum opacity and used to advantage the fact that $\sigma_{He\,I} \simeq \sigma_{He\,II}$ below 228 Å. Resulting hydrogen column densities are summarized in Table 3 for two AIA channels where the latter approximation holds best. However, this result looks very surprising. The obtained

column density, divided by a characteristic thickness of 5000 km (Table 2), is about two orders of magnitude lower than the hydrogen densities derived in the *same loops* from other diagnostics like optical-line inversions (Koza et al. 2019) or from white-light emission detected by SDO/HMI (Jejčič et al. 2018). Such density will be even lower if we add the hydrogen Lyman-continuum opacity to evaluation of total τ, or, if we use less bright hot loops with I_{BL1} as the background radiation. The reason for such a large discrepancy lies in improper application of the absorption model. While in the case of prominences only the absorption of the background radiation plays a major role, in cool flare loops we detect an extra emission $I_{DL} - I_f$ which, as demonstrated in this study, is not a partially absorbed background radiation because we know from independent diagnostics that the opacity is very large. Low values of τ obtained from the absorption model are thus an artifact of ignoring emission sources such as the continuum radiation discussed in this Letter or EUV line emission by weak hot loops in front of the cool ones.

As discussed by Anzer & Heinzel (2005), the so-called *emissivity deficit* (or formerly called a volume blocking) can play a role in the absorption model in the case of prominence structures significantly extended along the line of sight. This may generally apply also to an arcade of flare loops seen off-limb, but a detailed geometry is difficult to assess due to extreme complexity of the coronal emission. However, an emissivity deficit would play no role in the case of our dark loops, which are so opaque that the background radiation is totally absorbed. It may only have some effect on determination of the foreground coronal intensity I_f, but this is rather negligible.

6. Discussion and Conclusions

Our analysis of SDO/AIA cool loops seen in absorption shows that in the case of dense cool flare loops the standard absorption model leads to unrealistic underestimation of the opacity (optical thickness), and thus the plasma density, by almost two orders of magnitude. A large opacity was derived from the best-fit inversion model of the same loops obtained by Koza et al. (2019). This means that the background radiation is totally absorbed. To understand the nature of the radiation detected in dark AIA loops, we tested six loop models and estimated the level of the helium recombination continuum in all channels. While in channel 211 Å the observed signal can be represented by some models, in other channels the synthetic observables are much lower compared to the AIA signal. Our interpretation is that while the 211 Å channel may be dominated by the helium continuum in some cases, other channels show emission that seems to be due to weak hot loops projected against the dark ones—note that the whole loop arcade is rotated with respect to the line of sight (Kuridze et al. 2019). This is similar to observations of on-disk flares (Milligan et al. 2012; Milligan & McElroy 2013), where the ribbons produce the helium continuum that is visible close to continuum ionization edges at 504 and 228 Å, but further from them strong EUV lines and free–free continuum dominate. There exists also a possibility that the helium continuum itself is enhanced in a foreground hotter (transition-region) plasma because it is strongly dependent on plasma temperature—we see such a transition region in 1700 Å channel. We also

compared our model results with the AIA signal in 335 Å band and the result is similar to other channels below 200 Å. The He I recombination continuum seems to be again dominated by other EUV emissions. Our analysis thus suggests that we may detect the helium recombination continuum only in the 211 Å band.

The fact that we detect certain amount of radiation in otherwise totally absorbing cool loops affects the standard absorption model, leading to spurious values of τ. Such low values are the artifact of ignoring such emission in the standard model, and thus this model is inapplicable to cool flare loops with high density, contrary to the case of quiescent prominences. This might also be a reason why the empirical τ in Table 1 does not decrease with decreasing wavelength as expected.

As the reader can see, the quantitative analysis using the SDO/AIA data is rather cumbersome due to calibration issues and also due to inability to distinguish between the continuum and EUV line contributions to the AIA signals. In future work we will explore the possibility of using spectra of these loops taken by Hinode/EIS. In Table 2 we show the intensities at 211 Å, which is around the limit of shorter-wavelength band of EIS where Young et al. (2007) detected helium continuum in an active region. We will also make a more detailed non-LTE diagnostics, focusing on the helium continuum formation with a complex behavior of EUV photoionization by the surrounding arcade of hot flaring loops and using the up-to-date helium atomic data.

ORCID iDs

Petr Heinzel ⓘ https://orcid.org/0000-0002-5778-2600
Pavol Schwartz ⓘ https://orcid.org/0000-0001-5986-9948
Juraj Lörinčík ⓘ https://orcid.org/0000-0002-9690-8456
Július Koza ⓘ https://orcid.org/0000-0002-7444-7046
Sonja Jejčič ⓘ https://orcid.org/0000-0001-8489-4037
David Kuridze ⓘ https://orcid.org/0000-0003-2760-2311

References

Anzer, U., & Heinzel, P. 2005, ApJ, 622, 714
Avrett, E. H., Vernazza, J. E., & Linsky, J. L. 1976, ApJL, 207, L199
Boerner, P., Edwards, C., Lemen, J., et al. 2012, SoPh, 275, 41
Freeland, S. L., & Handy, B. N. 1998, SoPh, 182, 497

Heasley, J. N., Mihalas, D., & Poland, A. I. 1974, ApJ, 192, 181
Heinzel, P. 1995, A&A, 299, 563
Hubeny, I., & Mihalas, D. 2015, Theory of Stellar Atmospheres (Princeton, NJ: Princeton Univ. Press)
Jejčič, S., Kleint, L., & Heinzel, P. 2018, ApJ, 867, 134
Koza, J., Kuridze, D., Heinzel, P., et al. 2019, ApJ, 885, 154
Kucera, T. A. 2015, in Solar Prominences, Astrophysics and Space Science Library, Vol. 415, ed. J.-C. Vial & O. Engvold (Cham: Springer), 79
Kuridze, D., Mathioudakis, M., Morgan, H., et al. 2019, ApJ, 874, 126
Labrosse, N. 2015, in Solar Prominences, Astrophysics and Space Science Library, Vol. 415, ed. J.-C. Vial & O. Engvold (Cham: Springer), 131
Labrosse, N., & Gouttebroze, P. 2001, A&A, 380, 323
Labrosse, N., Schmieder, B., Heinzel, P., & Watanabe, T. 2011, A&A, 531, A69

Lemen, J. R., Title, A. M., Akin, D. J., et al. 2012, SoPh, 275, 17
Linsky, J. L., Glackin, D. L., Chapman, R. D., Neupert, W. M., & Thomas, R. J. 1976, ApJ, 203, 509
Lucy, L. B. 1974, AJ, 79, 745
Mihalas, D., & Stone, M. E. 1968, ApJ, 151, 293
Milligan, R. O., Chamberlin, P. C., Hudson, H. S., et al. 2012, ApJL, 748, L14
Milligan, R. O., & McElroy, S. A. 2013, ApJ, 777, 12
Pesnell, W. D., Thompson, B. J., & Chamberlin, P. C. 2012, SoPh, 275, 3
Poduval, B., DeForest, C. E., Schmelz, J. T., & Pathak, S. 2013, ApJ, 765, 144
Richardson, W. H. 1972, JOSA, 62, 55
Rumph, T., Bowyer, S., & Vennes, S. 1994, AJ, 107, 2108
Song, Q., Wang, J.-S., Feng, X., & Zhang, X. 2016, ApJ, 821, 83
Young, P. R., del Zanna, G., Mason, H. E., et al. 2007, PASJ, 59, S727